

Mid-infrared spectrally-pure single-photon states generation from 22 nonlinear optical crystals

Wu-Hao Cai^{1,2,3}, Ying Tian¹, and Rui-Bo Jin^{1,4*}

¹*Hubei Key Laboratory of Optical Information and Pattern Recognition,
Wuhan Institute of Technology, Wuhan 430205, China*

²*Research Institute of Electrical Communication,
Tohoku University, 2-1-1 Katahira, Sendai, 980-8577, Japan*

³*Graduate School of Engineering, Tohoku University,
6-6 Aramaki Aza Aoba, Aoba-ku, Sendai, 980-8579, Japan and*

⁴*Guangdong Provincial Key Laboratory of Quantum Science and Engineering,
Southern University of Science and Technology, Shenzhen 518055, China*

(Dated: March 24, 2023)

We theoretically investigate the preparation of pure-state single-photon source from 14 birefringent crystals (CMTC, TH1, LiIO₃, AAS, HGS, CGA, TAS, AGS, AGSe, GaSe, LIS, LISe, LGS, and LGSe) and 8 periodic poling crystals (LT, LN, KTP, KN, BaTiO₃, MgBaF₄, PMN-0.38PT, and OP-ZnSe) in a wavelength range from 1224 nm to 11650 nm. The three kinds of group-velocity-matching (GVM) conditions, the phase matching conditions, the spectral purity, and the Hong-Ou-Mandel interference are calculated for each crystal. This study may provide high-quality single-photon sources for quantum sensing, quantum imaging, and quantum communication applications at the mid-infrared wavelength range.

I. INTRODUCTION

Single-photon source at mid-infrared (MIR) wavelength range (approximately 2–20 μm) has important potential applications in quantum sensing, quantum imaging, and quantum communication [1–4]. Firstly, the 3–5 μm band contains absorption peaks of many gases, such as H₂O, CO, CO₂, SO₂, and SO₃ [5], so this band is important for sensing of these gases in environmental monitoring [6, 7]; the 7–10 μm band contains absorption peaks of H₂O₂, CH₄, O₃, TAT, Acetone, and sarin [5], etc, therefore this band is important for the sensing chemical or explosive materials in the applications of industrial production or defense security. The single-photon source in these gas sensing applications may provide an ultra-high sensitivity [8]. Secondly, 3–5 μm and 8–14 μm are two widely used ranges for MIR thermal infrared imaging camera for medical and forensic usage [9], since the room temperature objects emit light at these wavelength ranges. And MIR single-photon sources can provide a diagnosis in a non-invasive manner, which is important for medical or biological samples [10]. Thirdly, 3–5 μm is also an atmospheric transmission window with relatively high transparency, which is useful for large-scale free-space quantum communications, such as entanglement distribution [11], quantum key distribution [12], or quantum direct communication [13].

Spontaneous parametric down-conversion (SPDC) and four-wave mixing (FWM) are two widely used methods to prepare single photons. Many previous works have been dedicated to the development of high-quality single-photon source or entangled photon source in the MIR

range from an SPDC or FWM process. On the experimental side, PPLN [14–16], GaP [17], and silicon waveguide [18] have been investigated to prepare single-photon source; PPLN [19] has been studied for entangled photon source generation. On the theory side, PPLN [20], PPKN [21], PMN-0.38PT [22], etc have been investigated for single-photon source [23–27]; p-doped semiconductor [28] has been studied for entangled photon source. In addition, some studies explored single-photon detection by superconducting nanowire single-photon detector (SNSPD) [29–31] or by silicon avalanche photodiode (SAPD) in an up-conversion configuration [14, 32].

However, the previous studies are still insufficient for the need of MIR applications. On one hand, the previous experimental work is mainly focused on PPLN crystal and the wavelength range is below 5 μm . SO, the range from 5–20 μm is still needs further exploration. On the other hand, the spectrally-pure single photon source is proved to be a good resource [33], but this source is still rare because the group-velocity matching (GVM) conditions can only be matched at very limited wavelengths in a crystal. Therefore, it is still necessary to explore more nonlinear optical crystals to fully meet the need of MIR band applications. For this purpose, in this work, we investigate MIR spectrally-pure single-photon generation from 14 crystals by the birefringence phase matching (BPM) method, and 8 crystals by the quasi-phase-matching (QPM) method. They can meet three kinds of GVM conditions and prepare spectrally uncorrelated biphotons so as to generate spectrally pure heralded single-photon state.

* jrbqyj@gmail.com

Name (Ref.)	chemical formula	axis	point group	$\lambda_{transp.}$ (μm)	$d_{max(wavelength)}$ (pm/V)
CMTC	$\text{CdHg}(\text{SCN})_4$	uniaxial	4	0.40~2.35	$d_{31(1.064)} = 6.2 \pm 1.2$
THI	Tl_4HgI_6	uniaxial	4mm	1.00~60.0	unknown
LiIO_3 [34]	LiIO_3	uniaxial	6	0.28~6.00	$d_{33(1.064)} = 4.6 \pm 0.3$
AAS	Ag_3AsS_3	uniaxial	3m	0.61~13.3	$d_{22(1.064)} = 16.6 \pm 2.5$
HGS [35]	HgGa_2S_4	uniaxial	4	0.55~13.0	$d_{36(1.064)} = 31.5 \pm 4.7$
CGA [36]	CdGeAs_2	uniaxial	$\bar{4}2\text{m}$	2.30~18.0	$d_{36(10.6)} = 186 \pm 16$
TAS	Tl_3AsSe_3	uniaxial	3m	1.28~17.0	$d_{+(10.6)} = 68 \pm 31$
AGS	AgGaS_2	uniaxial	$\bar{4}2\text{m}$	0.47~13.0	$d_{36(10.6)} = 12.5 \pm 2.5$
AGSe	AgGaSe_2	uniaxial	$\bar{4}2\text{m}$	0.71~19.0	$d_{36(10.591)} = 39.5 \pm 1.9$
GaSe [37]	GaSe	uniaxial	62m	0.62~20.0	$d_{22(10.6)} = 54 \pm 11$ [37]
LIS [38]	LiInS_2	biaxial	mm2	0.34~13.2	$d_{33(2.3)} = -16 \pm 4$
LISE [39]	LiInSe_2	biaxial	mm2	0.46~14.0	$d_{31(2.3)} = -16 \pm 4$ [40]
LGS [41]	LiGaS_2	biaxial	mm2	0.32~11.6	$d_{33(2.3)} = -10.7 \pm 2.7$ [42]
LGSe [43]	LiGaSe_2	biaxial	mm2	0.37~13.2	$d_{33(2.3)} = -18.2 \pm 4.6$ [42]
LT [44]	LiTaO_3	uniaxial	3m	0.28~5.50	$d_{33(1.064)} = 12.9$
LN	LiNbO_3	uniaxial	3m	0.40~5.50	$d_{33(1.064)} = 25.2$
KTP	KTiOPO_4	biaxial	mm2	0.35~4.50	$d_{33(1.064)} = 14.6 \pm 0.7$
KN	KNbO_3	biaxial	mm2	0.40~4.50	$d_{11(1.064)} = 21.9 \pm 0.5$ [45]
BaTiO_3	BaTiO_3	uniaxial	4mm (room temp.)	0.40~9.00	$d_{32(1.06)} = 14.4 \pm 2.5$
MgBaF_4	MgBaF_4	biaxial	mm2	0.14~10.0	$d_{32(1.064)} = 0.039$
PMN-0.38PT [46]	$0.62\text{Pb}(\text{Mg}_{1/3}\text{Nb}_{2/3})\text{O}_3 - 0.38\text{PbTiO}_3$	uniaxial	4mm	0.3~11.0	$^\dagger d_{33(1.064)} = 12.6$
OP-ZnSe [47]	ZnSe	isotropic	$\bar{4}3\text{m}$	0.45~18.0	$d_{36(0.852)} = 53.8$

TABLE I. Main properties of the 10 uniaxial birefringent crystals (part I), 4 biaxial birefringent crystals (part II), and 8 periodic poling crystals (part III) discussed in this work, including the chemical formula, the axis (uniaxial, biaxial, or isotropic), the point group, the transparency range $\lambda_{transp.}$, and the maximal nonlinear coefficient d_{max} at different wavelength (in μm in the bracket). Most of the data were obtained from Refs. [48, 49]. The BaTiO_3 crystal has different types of point group at different temperatures. * $d_+ = |d_{31}\sin\theta| + |d_{22}\cos\theta|$. † The calculated result is from [22] according to the method from [50].

II. THEORY

A. The characteristics of 22 kinds of nonlinear crystals

We investigate 22 kinds of nonlinear crystals in this work. Table I summarizes them from several perspectives: axial type, point group, transparency range, and the maximal nonlinear coefficient. We separate these crystals into three categories by their axial type or phase-matching form in order to illustrate the result more clearly in the next section. Most Sellmeier equations were obtained from Refs. [48, 49], and we have updated some Sellmeier equations with the latest references and concluded in Tab.I.

In the first category, 9 birefringent uniaxial crystals are listed in the table. They have a very large transparency range up to 20 μm except CMTC and LiIO_3 . We show 4 birefringent biaxial crystals in the second category, these four crystals can be written as LiMX ($M = \text{In, Ga}$ and $X = \text{S, Se}$). Here, In and Ga are elements of group IIIA in the periodic table; S and Se are elements of group VIA. They are all mm2 point group. With their transparency range up to 14 μm , they have similar properties and can perform many applications in the MIR band. The other 8 periodic poling crystals usually realize their phase-matching by the QPM method, so we discuss them

in the section III B and IV in detail.

B. The GVM theory of spectrally-pure single-photon states generation

The SPDC process generates the biphoton state $|\psi\rangle$, which can be written as

$$|\psi\rangle = \int_0^\infty \int_0^\infty d\omega_s d\omega_i f(\omega_s, \omega_i) \hat{a}_s^\dagger(\omega_s) \hat{a}_i^\dagger(\omega_i) |0\rangle|0\rangle, \quad (1)$$

where \hat{a}^\dagger is the creation operator; ω is the angular frequency, and the subscripts s and i denote the signal and idler photon. The joint spectral amplitude (JSA) $f(\omega_s, \omega_i)$ can be obtained by multiplying the pump envelope function (PEF) $\alpha(\omega_s, \omega_i)$ and the phase matching function (PMF) $\phi(\omega_s, \omega_i)$, i.e., $f(\omega_s, \omega_i) = \alpha(\omega_s, \omega_i) \times \phi(\omega_s, \omega_i)$.

For PEF, it is usually a Gaussian distribution and can be expressed as [51],

$$\alpha(\omega_s, \omega_i) = \exp\left[-\frac{1}{2} \left(\frac{\omega_s + \omega_i - \omega_{p0}}{\sigma_p}\right)^2\right], \quad (2)$$

where σ_p is the bandwidth of the pump; ω_{p0} is the center frequency of the pump; the full-width at half-maximum (FWHM) is $\text{FWHM}_\omega = 2\sqrt{\ln(2)}\sigma_p \approx 1.67\sigma_p$.

If we use wavelengths as the variable by $\omega = 2\pi c/\lambda$ for ease of calculation, the PEF can be rewritten as

$$\alpha(\lambda_s, \lambda_i) = \exp \left\{ -\frac{1}{2} \left(\frac{1/\lambda_s + 1/\lambda_i - 1/(\lambda_0/2)}{\Delta\lambda/[(\lambda_0/2)^2 - (\Delta\lambda/2)^2]} \right)^2 \right\}, \quad (3)$$

where $\lambda_0/2$ is the central wavelength of the pump; $\Delta\lambda$ is the bandwidth of wavelength and $\sigma_p = \frac{2\pi c}{\Delta\lambda/[(\lambda_0/2)^2 - (\Delta\lambda/2)^2]}$, where c is the light speed.

For $\Delta\lambda \ll \lambda_0$, The FWHM of the pump at intensity level is $\text{FWHM}_\lambda \approx 2\sqrt{\ln(2)}\Delta\lambda \approx 1.67\Delta\lambda$.

By assuming a flat phase distribution, the PMF can be written as an *sinc* function shape [51],

$$\phi(\omega_s, \omega_i) = \text{sinc} \left(\frac{\Delta k L}{2} \right), \quad (4)$$

where L is the length of crystal, Δk is the wave vector mismatch. For QPM case, $\Delta k = k_p - k_i - k_s \pm \frac{2\pi}{\Lambda}$, and $k = \frac{2\pi n(\lambda)}{\lambda}$ is the wave vector. The refractive index $n(\lambda)$ is a function of wavelength λ . Λ is the poling period, and $\Lambda = \frac{2\pi}{|k_p - k_i - k_s|}$. For BPM case, $\Delta k = k_p - k_i - k_s$, and $k = \frac{2\pi n(\lambda, \theta, \varphi)}{\lambda}$. For ordinary ray (o-ray), the refractive index $n_o(\lambda)$ is a function of wavelength λ . While for extraordinary ray (e-ray), the refractive index $n_e(\lambda, \theta, \varphi)$ is a function of polar angle θ , azimuth angle φ and wavelength λ .

According to the refractive index coordinate in Appendix of Ref. [52], θ is the polar angle between the optical axis of the crystal and the light propagation direction, φ is the azimuth angle in the xy plane. For uniaxial crystals, θ is the cutting angle of the crystals. For biaxial crystals, when light propagates in the xz plane, $\varphi=0^\circ$, θ is the cutting angle; when light propagates in the yz plane, $\varphi=90^\circ$, θ is the cutting angle; when light propagates in the xy plane, $\theta=90^\circ$, φ is the cutting angle.

When the $\Delta k=0$, the phase-matching condition is satisfied. Under on this precondition, we consider the GVM condition to prepare an intrinsic spectrally-pure state. The angle θ_{PMF} between the positive direction of the horizontal axis and the ridge direction of the PEF is determined by [53]:

$$\tan(\theta_{PMF}) = - \left(\frac{V_{g,p}^{-1}(\omega_p) - V_{g,s}^{-1}(\omega_s)}{V_{g,p}^{-1}(\omega_p) - V_{g,i}^{-1}(\omega_i)} \right), \quad (5)$$

where $V_{g,\mu} = \frac{d\omega}{dk_\mu(\omega)} = \frac{1}{k'_\mu(\omega)}$, ($\mu = p, s, i$) is the group velocity of the pump, the signal and the idler.

We consider three kinds of GVM conditions [54]. The GVM₁ condition ($\theta_{PMF} = 0^\circ$) is

$$V_{g,p}^{-1}(\omega_p) = V_{g,s}^{-1}(\omega_s). \quad (6)$$

The GVM₂ condition ($\theta_{PMF} = 90^\circ$) is

$$V_{g,p}^{-1}(\omega_p) = V_{g,i}^{-1}(\omega_i). \quad (7)$$

The GVM₃ condition ($\theta_{PMF} = 45^\circ$) is

$$2V_{g,p}^{-1}(\omega_p) = V_{g,s}^{-1}(\omega_s) + V_{g,i}^{-1}(\omega_i). \quad (8)$$

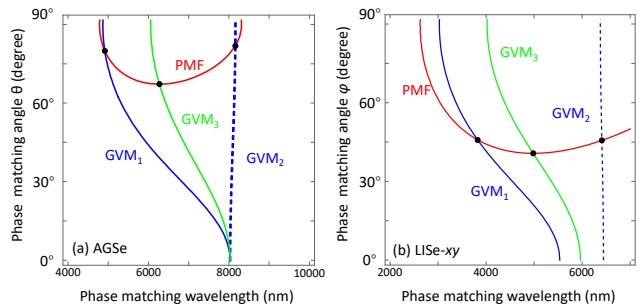


FIG. 1. The phase-matching function and group-velocity matching functions (GVM_{1(2,3)}) for different signal/idler wavelength and phase-matching angle (polar angle) θ for AGSe crystal (a) and phase-matching (azimuth angle) angle φ for LISe crystal in the xy plane (b). In this calculation, we consider the Type-II phase-matching condition with collinear and wavelength-degenerate ($2\lambda_p = \lambda_s = \lambda_i$) configuration.

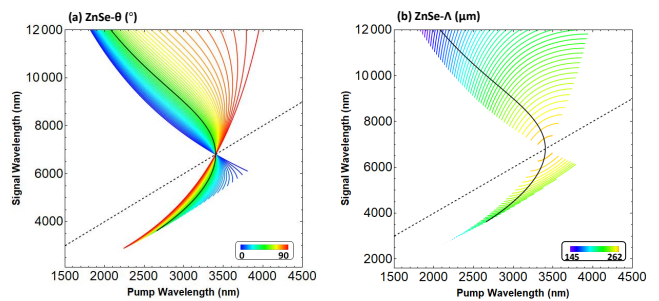


FIG. 2. (a, b): The GVM angle θ_{PMF} and the corresponding poling period Λ for QPM crystal OP-ZnSe. The solid black line indicates $\theta_{PMF} = 45^\circ$, and the dashed black line indicates the degenerate case $2\lambda_p = \lambda_s$. In this figure, the QPM non-degenerate wavelengths case is under type-0 phase-matching condition.

The pure state not only can be prepared through these three GVM conditions but also all the conditions that the θ_{PMF} angles are between 0 and 90° [55, 56]. Since these three GVM conditions are listed in Eqs. (6-8) are the most widely-used cases in the experiment, we mainly consider these three conditions within this work. Besides, the degenerate or nondegenerate case of other θ_{PMF} under type-II and type-0 phase-matching conditions will be illustrated in section III C.

III. CALCULATION AND SIMULATION

A. Birefringent crystals

Firstly, we consider the birefringent crystals with the BPM method. We assume the wavelength is degenerated, i.e., $2\lambda_p = \lambda_s = \lambda_i$. For uniaxial crystals, negative uniaxial crystals satisfy the type-II SPDC with $e \rightarrow o+e$ phase-matching interaction. Here the pump and idler are extraordinary (e) beams, while the signal is ordinary

Name	GVM ₁ (purity ≈ 0.97)	GVM ₂ (purity ≈ 0.97)	GVM ₃ (purity ≈ 0.82)
CMTC*	$\lambda_p = 649$ nm, $\lambda_{s,i} = 1298$ nm $\theta = 41.2^\circ$, $d_{\text{eff}} = -4.46$ pm/V	$\lambda_p = 1156$ nm, $\lambda_{s,i} = 2312$ nm $\theta = 43.6^\circ$, $d_{\text{eff}} = -3.63$ pm/V	$\lambda_p = 829$ nm, $\lambda_{s,i} = 1658$ nm $\theta = 38.2^\circ$, $d_{\text{eff}} = -4.13$ pm/V
THI [†]	$\lambda_p = 2841$ nm, $\lambda_{s,i} = 5682$ nm $\theta = 29.3^\circ$, $d_{\text{eff}} = \text{unknown}$	$\lambda_p = 4822$ nm, $\lambda_{s,i} = 9644$ nm $\theta = 29.3^\circ$, $d_{\text{eff}} = \text{unknown}$	$\lambda_p = 3705$ nm, $\lambda_{s,i} = 7410$ nm $\theta = 27.2^\circ$, $d_{\text{eff}} = \text{unknown}$
LiIO ₃	$\lambda_p = 835$ nm, $\lambda_{s,i} = 1670$ nm $\theta = 29.3^\circ$, $d_{\text{eff}} = 0.09$ pm/V	$\lambda_p = 1460$ nm, $\lambda_{s,i} = 2920$ nm $\theta = 29.7^\circ$, $d_{\text{eff}} = 0.09$ pm/V	$\lambda_p = 1088$ nm, $\lambda_{s,i} = 2176$ nm $\theta = 27.2^\circ$, $d_{\text{eff}} = 0.09$ pm/V
AAS	$\lambda_p = 2151$ nm, $\lambda_{s,i} = 4302$ nm $\theta = 22.3^\circ$, $d_{\text{eff}} = 0.16$ pm/V	$\lambda_p = 3617$ nm, $\lambda_{s,i} = 7234$ nm $\theta = 22.3^\circ$, $d_{\text{eff}} = 0.15$ pm/V	$\lambda_p = 2793$ nm, $\lambda_{s,i} = 5586$ nm $\theta = 20.7^\circ$, $d_{\text{eff}} = 0.16$ pm/V
HGS	$\lambda_p = 1704$ nm, $\lambda_{s,i} = 3408$ nm $\theta = 60.1^\circ$, $d_{\text{eff}} = 0.29$ pm/V	$\lambda_p = 2819$ nm, $\lambda_{s,i} = 5638$ nm $\theta = 59.8^\circ$, $d_{\text{eff}} = 0.29$ pm/V	$\lambda_p = 2206$ nm, $\lambda_{s,i} = 4412$ nm $\theta = 54.2^\circ$, $d_{\text{eff}} = 0.32$ pm/V
CGA	$\lambda_p = 3692$ nm, $\lambda_{s,i} = 7384$ nm $\theta = 54.6^\circ$, $d_{\text{eff}} = 0.02$ pm/V	$\lambda_p = 5825$ nm, $\lambda_{s,i} = 11650$ nm $\theta = 53.9^\circ$, $d_{\text{eff}} = 0.02$ pm/V	$\lambda_p = 4690$ nm, $\lambda_{s,i} = 9380$ nm $\theta = 49.8^\circ$, $d_{\text{eff}} = 0.02$ pm/V
TAS	$\lambda_p = 3620$ nm, $\lambda_{s,i} = 7240$ nm $\theta = 27.5^\circ$, $d_{\text{eff}} = 0.24$ pm/V	$\lambda_p = 5535$ nm, $\lambda_{s,i} = 11070$ nm $\theta = 27.0^\circ$, $d_{\text{eff}} = 0.23$ pm/V	$\lambda_p = 4570$ nm, $\lambda_{s,i} = 9140$ nm $\theta = 25.6^\circ$, $d_{\text{eff}} = 0.24$ pm/V
AGS	$\lambda_p = 1688$ nm, $\lambda_{s,i} = 3376$ nm $\theta = 53.7^\circ$, $d_{\text{eff}} = 0.14$ pm/V	$\lambda_p = 2845$ nm, $\lambda_{s,i} = 5690$ nm $\theta = 53.9^\circ$, $d_{\text{eff}} = 0.14$ pm/V	$\lambda_p = 2187$ nm, $\lambda_{s,i} = 4374$ nm $\theta = 48.9^\circ$, $d_{\text{eff}} = 0.15$ pm/V
AGSe	$\lambda_p = 2457$ nm, $\lambda_{s,i} = 4914$ nm $\theta = 79.9^\circ$, $d_{\text{eff}} = 0.11$ pm/V	$\lambda_p = 4079$ nm, $\lambda_{s,i} = 8158$ nm $\theta = 81.9^\circ$, $d_{\text{eff}} = 0.13$ pm/V	$\lambda_p = 3136$ nm, $\lambda_{s,i} = 6272$ nm $\theta = 67.2^\circ$, $d_{\text{eff}} = 0.25$ pm/V
GaSe	$\lambda_p = 2189$ nm, $\lambda_{s,i} = 4378$ nm $\theta = 16.1^\circ$, $d_{\text{eff}} = 0.51$ pm/V	$\lambda_p = 3657$ nm, $\lambda_{s,i} = 7314$ nm $\theta = 16.1^\circ$, $d_{\text{eff}} = 0.49$ pm/V	$\lambda_p = 2833$ nm, $\lambda_{s,i} = 5666$ nm $\theta = 15.0^\circ$, $d_{\text{eff}} = 0.51$ pm/V

TABLE II. Three kinds of GVM conditions for 10 uniaxial BPM crystals. $\lambda_{p(s,i)}$ is the GVM wavelength for the pump (signal, idler). θ is the phase-matching angle and d_{eff} is the effective nonlinear coefficient. The Sellmeier equations are obtained from Refs. [48, 49]. Most of the d_{eff} values can be obtained from the SNLO *v78* software package, developed by AS-Photonics, LLC [57]. *The d_{eff} value for CMTC is not available from SNLO, we have calculated the d_{eff} using the method in the Appendix of Ref. [52] and considering Miller's rule [58]. [†] The d_{eff} value for THI is unknown.

Name	GVM ₁ (purity ≈ 0.97)	GVM ₂ (purity ≈ 0.97)	GVM ₃ (purity ≈ 0.82)
LIS- <i>xy</i>	$\lambda_p = 1457$ nm, $\lambda_{s,i} = 2914$ nm $\varphi = 56.7^\circ$, $d_{\text{eff}} = 6.01$ pm/V	$\lambda_p = 2473$ nm, $\lambda_{s,i} = 4946$ nm $\varphi = 56.7^\circ$, $d_{\text{eff}} = 5.74$ pm/V	$\lambda_p = 1901$ nm, $\lambda_{s,i} = 3802$ nm $\varphi = 49.5^\circ$, $d_{\text{eff}} = 6.05$ pm/V
LISe- <i>xy</i>	$\lambda_p = 1912$ nm, $\lambda_{s,i} = 3824$ nm $\varphi = 45.8^\circ$, $d_{\text{eff}} = 9.65$ pm/V	$\lambda_p = 3205$ nm, $\lambda_{s,i} = 6410$ nm $\varphi = 45.6^\circ$, $d_{\text{eff}} = 9.31$ pm/V	$\lambda_p = 2491$ nm, $\lambda_{s,i} = 4982$ nm $\varphi = 40.7^\circ$, $d_{\text{eff}} = 9.19$ pm/V
LGS- <i>xy</i>	$\lambda_p = 1347$ nm, $\lambda_{s,i} = 2696$ nm $\varphi = 55.5^\circ$, $d_{\text{eff}} = 5.24$ pm/V	$\lambda_p = 2282$ nm, $\lambda_{s,i} = 4564$ nm $\varphi = 55.1^\circ$, $d_{\text{eff}} = 5.02$ pm/V	$\lambda_p = 1767$ nm, $\lambda_{s,i} = 3534$ nm $\varphi = 49.7^\circ$, $d_{\text{eff}} = 5.19$ pm/V
LGSe- <i>xy</i>	$\lambda_p = 1641$ nm, $\lambda_{s,i} = 3282$ nm $\varphi = 47.8^\circ$, $d_{\text{eff}} = 8.37$ pm/V	$\lambda_p = 2729$ nm, $\lambda_{s,i} = 5258$ nm $\varphi = 47.5^\circ$, $d_{\text{eff}} = 8.06$ pm/V	$\lambda_p = 2129$ nm, $\lambda_{s,i} = 4258$ nm $\varphi = 43.3^\circ$, $d_{\text{eff}} = 8.38$ pm/V

TABLE III. Three kinds of GVM conditions for 4 biaxial BPM crystals with light propagating in the *xy* plane. φ is the azimuth angle. The d_{eff} are obtained from SNLO *v78* [57].

(o) beam. In contrast, the positive uniaxial crystals can meet the Type-II SPDC with $o \rightarrow o+e$ phase-matching interaction. Note all the simulations are based on collinear figuration.

10 kinds of uniaxial crystals are investigated in this work. Taking AgSe crystal as an example, we plot the PMF and GVM_{1(2,3)} conditions for different wavelengths and phase-matched angles in Fig. 1 (a). The PMF (red) crosses the GVM_{1(2,3)} (blue and green) at three black points, which meet the PMF and three kinds of GVM conditions simultaneously. The three points associated with wavelengths of 4914, 8158, and 6272 nm, respectively, and angles of 79.9°, 81.9°, and 67.2°. Further, we calculate the other uniaxial crystals with the same method, and then we summarize the result in Table II. In Table II, the down-converted photons have a wavelength range from 1298 to 11650 nm, which is in the

near-infrared (NIR) and MIR bands. The corresponding spectral purity at GVM_{1(2,3)} wavelengths is 0.97, 0.97, and 0.82, respectively.

For biaxial crystals, all the crystals we investigated can only satisfy the GVM conditions in the *xy* plane, with polar angle $\theta = 90^\circ$. We study 4 kinds of biaxial crystals and choose the LISe crystal as an example, which represents the mm2 point group. The assignment of dielectric and crystallographic axes are X, Y, Z \Rightarrow b, a, c. As shown in Fig. 1 (b), in the *xy* plane the cross points reflect the GVM condition can be fulfilled at the wavelength of 3824, 6410, and 4982 nm, respectively.

All the biaxial crystals can prepare pure-state in the range from 2696 to 6410 nm in Tab. III. We can notice that the wavelength range is from 1298 to 7384 nm for the GVM₁ condition, from 2312 to 11650 nm for the GVM₂ condition, and from 1658 to 9380 nm for the GVM₃ con-

Name	GVM ₁ (purity ≈ 0.97)	GVM ₂ (purity ≈ 0.97)	GVM ₃ (purity ≈ 0.82)
LT	$\lambda_p = 1279$ nm, $\lambda_{s,i} = 2558$ nm $\Lambda = 33.7$ μm , $d_{\text{eff}} = 0.27$ pm/V	$\lambda_p = 1320$ nm, $\lambda_{s,i} = 2640$ nm $\Lambda = 33.7$ μm , $d_{\text{eff}} = 0.27$ pm/V	$\lambda_p = 1299$ nm, $\lambda_{s,i} = 2598$ nm $\Lambda = 33.7$ μm , $d_{\text{eff}} = 0.27$ pm/V
LN	$\lambda_p = 1341$ nm, $\lambda_{s,i} = 2682$ nm $\Lambda = 14.7$ μm , $d_{\text{eff}} = 2.70$ pm/V	$\lambda_p = 2015$ nm, $\lambda_{s,i} = 4030$ nm $\Lambda = 15.2$ μm , $d_{\text{eff}} = 2.50$ pm/V	$\lambda_p = 1709$ nm, $\lambda_{s,i} = 3418$ nm $\Lambda = 15.5$ μm , $d_{\text{eff}} = 2.60$ pm/V
KTP	$\lambda_p = 613$ nm, $\lambda_{s,i} = 1224$ nm $\Lambda = 70.2$ μm , $d_{\text{eff}} = 2.50$ pm/V	$\lambda_p = 1169$ nm, $\lambda_{s,i} = 2338$ nm $\Lambda = 72.2$ μm , $d_{\text{eff}} = 2.40$ pm/V	$\lambda_p = 792$ nm, $\lambda_{s,i} = 1584$ nm $\Lambda = 45.0$ μm , $d_{\text{eff}} = 2.40$ pm/V
KN	$\lambda_p = 1412$ nm, $\lambda_{s,i} = 2824$ nm $\Lambda = 6.2$ μm , $d_{\text{eff}} = 5.20$ pm/V	$\lambda_p = 1869$ nm, $\lambda_{s,i} = 3738$ nm $\Lambda = 6.1$ μm , $d_{\text{eff}} = 5.00$ pm/V	$\lambda_p = 1605$ nm, $\lambda_{s,i} = 3210$ nm $\Lambda = 6.3$ μm , $d_{\text{eff}} = 5.10$ pm/V
BaTiO ₃ *	$\lambda_p = 1518$ nm, $\lambda_{s,i} = 3036$ nm $\Lambda = 23.3$ μm , $d_{\text{eff}} = 10.13$ pm/V	$\lambda_p = 1993$ nm, $\lambda_{s,i} = 3986$ nm $\Lambda = 23.3$ μm , $d_{\text{eff}} = 9.17$ pm/V	$\lambda_p = 1740$ nm, $\lambda_{s,i} = 3480$ nm $\Lambda = 23.8$ μm , $d_{\text{eff}} = 9.69$ pm/V
MgBaF ₄ *	$\lambda_p = 989$ nm, $\lambda_{s,i} = 1978$ nm $\Lambda = 948.5$ μm , $d_{\text{eff}} = 0.04$ pm/V	not satisfied	$\lambda_p = 1390$ nm, $\lambda_{s,i} = 2780$ nm $\Lambda = 680.6$ μm , $d_{\text{eff}} = 0.04$ pm/V
PMN-0.38PT [†]	$\lambda_p = 2810$ nm, $\lambda_{s,i} = 5620$ nm $\Lambda = 1301.38$ μm , $d_{\text{eff}} = \text{unknown}$	not satisfied	$\lambda_p = 3972$ nm, $\lambda_{s,i} = 7944$ nm $\Lambda = 917.83$ μm , $d_{\text{eff}} = \text{unknown}$
OP-ZnSe		$\lambda_p = 3403$ nm, $\lambda_{s,i} = 6806$ nm $\Lambda = 262.97$ μm , $d_{\text{eff}} = 19.1$ pm/V	

TABLE IV. Three kinds of GVM conditions for 8 QPM crystals. $\lambda_{p(s,i)}$ is the GVM wavelength for the pump (signal, idler). Λ is the poling period and d_{eff} is the effective nonlinear coefficient. The Sellmeier equations are obtained from Refs. [48, 49]. Most of the d_{eff} values can be obtained from the SNLO *v78* software package, developed by AS-Photonics, LLC [57]. *The d_{eff} values for BaTiO₃ and MgBaF₄ are not available from SNLO, so we have calculated them using the method in the Appendix of Ref. [52] and considering Miller's rule [58]. [†] The d_{eff} value for PMN-0.38PT is unknown.

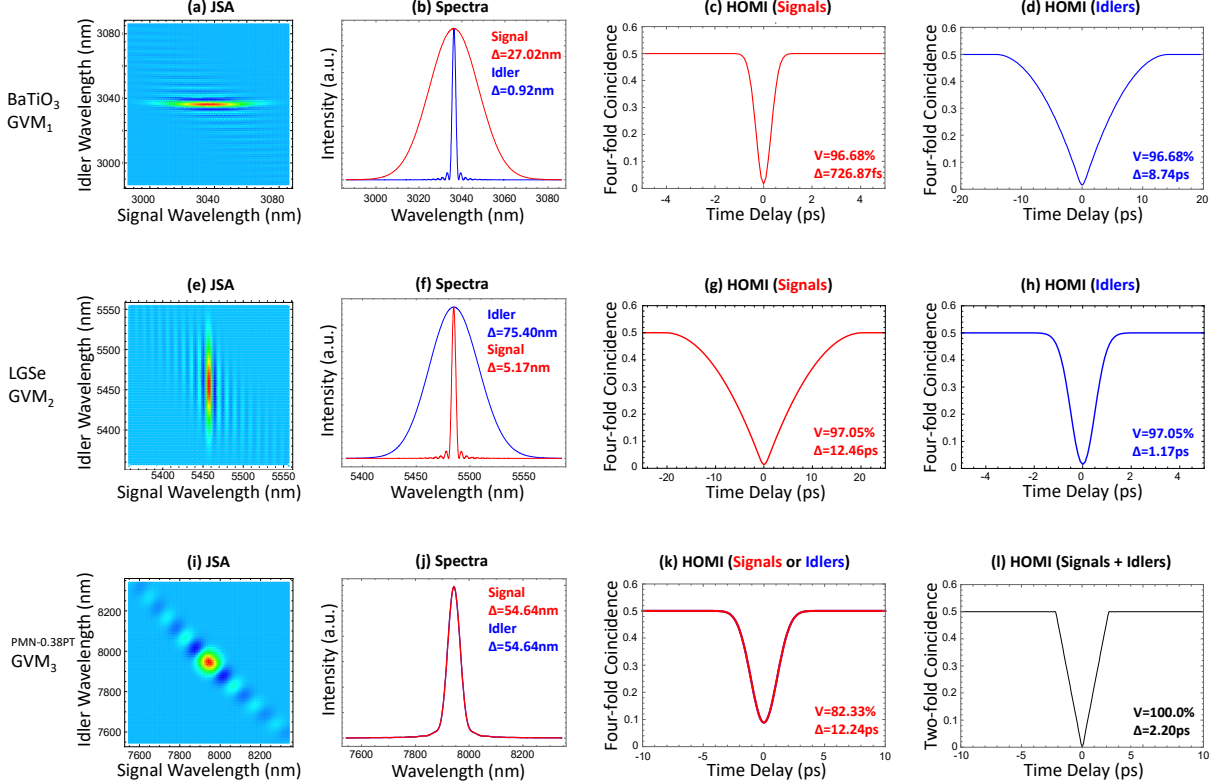


FIG. 3. (a, e, i) are the JSAs; (b, f, j) are the spectra; and (c, d, g, h, k, l) are the HOM interference patterns. The FWHM of the spectra (Δ) for the signal and the idler, the visibility (V) and the FWHM (Δ) of two-fold and four-fold HOM interference are shown in the figures. The parameters of $L = 100$ mm and $\Delta\lambda = 4$ nm (FWHM = 6.66 nm), $L = 200$ mm and $\Delta\lambda = 8$ nm (FWHM = 13.32 nm), $L = 100$ mm and $\Delta\lambda = 11$ nm (FWHM = 18.32 nm) are adopted for BaTiO₃, LGSe, and PMN-0.38PT, respectively. Note that for all the calculations of purity, we use a grid size of 200×200 for all the JSAs.

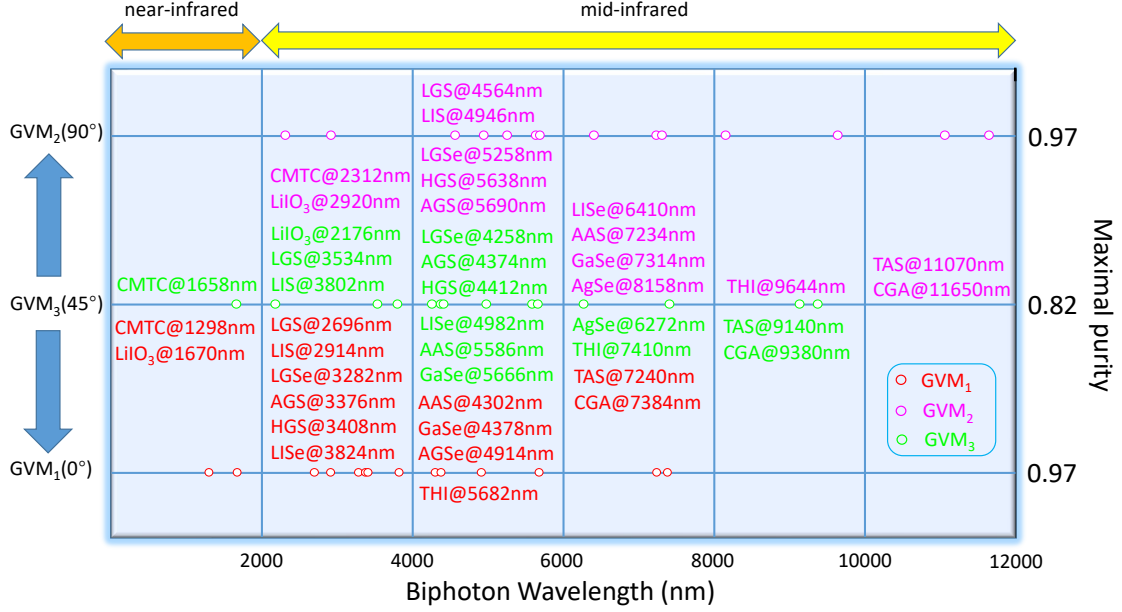


FIG. 4. The result of all the BPM crystals for three kinds of GVM conditions. GVM₁₍₂₎ can achieve a purity of 0.97. GVM₃ can achieve a purity of 0.82. The GVM angle increases from 0° to 45° and ends up at 90° on the left axis for GVM_{1(2,3)} condition. The GVM₁ condition (red points) can cover the wavelength range from 1298 nm to 7384 nm. The GVM₂ condition (magenta points) can cover the wavelength range from 2312 nm to 11650 nm. The GVM₃ condition (green points) can cover the wavelength range from 1658 nm to 9380 nm.

dition (also shown in Fig. 4), which can meet the different application demand in NIR, MIR, and telecom wavelengths.

B. Periodic poling crystals

In this section, we consider 8 periodic poling crystals with the QPM method, which has several advantages. For example, the largest component of the nonlinear coefficient matrix (usually d_{33}) can be utilized; there is no walk-off angle so as to achieve good spatial mode; it allows phase-matching interaction in isotropic media, in which the BPM is not applicable [59]. The GVM wavelengths, the poling period Λ , and the effective nonlinear coefficient d_{eff} are calculated and listed in Tab. IV. The LT, LN, KTP, and KN crystals are traditionally often-used QPM crystals [21, 60–62]. Here, we find the GVM₂ wavelengths are all above 2 μm .

The BaTiO₃ crystal shows a low birefringence, thus, only suitable for QPM method. With its high transmission in the IR range, it is possible to prepare pure-state at 3036, 3986, and 3480 nm, respectively. The MgBaF₄ crystal can meet the GVM₁ condition at 1978 nm, and the GVM₃ condition at 2780 nm. Note that this crystal does not satisfy the GVM₂ condition. The PMN-0.38PT is a functional ferroelectric material. The GVM condition only can be fulfilled at two wavelengths, i.e., 5620 nm and 7944 nm for GVM₁ and GVM₃ conditions. The orientation-patterned zinc selenide (OP-

ZnSe) is an isotropic semiconductor material, therefore, the QPM rather than BPM is applicable. OP-ZnSe has extremely high nonlinear coefficients. Since the crystal possesses only one refractive index, it can only perform type-0 SPDC, i.e., $e \rightarrow e+e$ interaction, which will be discussed in the next section. All the QPM crystals can prepare pure-state at the range from 1224 to 7944 nm, as listed in Tab. IV.

C. Wavelength nondegenerate case

In this section, we focus on the wavelength nondegenerate case using QPM method. We take OP-ZnSe as an example and calculate the θ_{PMF} in the range of 0 and 90 degrees and the corresponding poling period Λ in Fig. 2. The dashed black line in Fig. 2 indicates the degenerate case, i.e., $2\lambda_p = \lambda_s$. For one fixed pump wavelength, we can find θ_{PMF} and Λ of different signal wavelengths.

The OP-ZnSe crystal can only perform type-0 SPDC, i.e., $e \rightarrow e+e$ interaction. Under the degenerate condition, the signal and the idler have the same group velocity, so pure state can not be prepared. The lines of all the angles θ_{PMF} converge in one point. At this point, all the GVM conditions are satisfied synchronously. Due to the singularity caused by these GVM conditions, the degenerate case at this point does not provide high purity, while the pure state can be prepared in the other area of different θ_{PMF} .

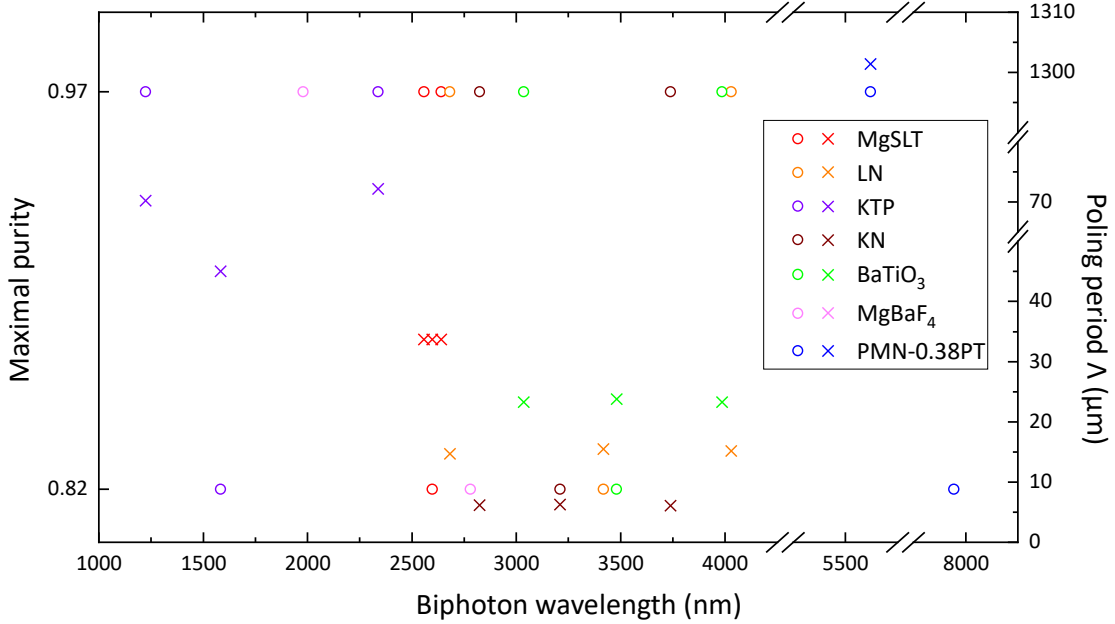


FIG. 5. The result of all the QPM crystals for three kinds of GVM conditions. $GVM_{1(2)}$ can achieve a purity of 0.97. GVM_3 can achieve a purity of 0.82. The wavelength versus achievable maximal spectral purity and poling period Λ can be reflected on the scale of the left and right Y-axis. The wavelength range is from 1224 nm to 7944 nm, and the poling period Λ is from 6.1 μm to 1301.38 μm

D. HOM interference simulation

The quality of the spectrally uncorrelated biphoton state can be tested by Hong-Ou-Mandel (HOM) interference. There are two kinds of HOM interference, the first one is the HOM interferences using signal and idler photons from the same SPDC source, with a typical setup shown in [63]. In this case, the two-fold coincidence probability $P_2(\tau)$ as a function of the time delay τ is given by [64–66]:

$$P_2(\tau) = \frac{1}{4} \int_0^\infty \int_0^\infty d\omega_s d\omega_i \left| [f(\omega_s, \omega_i) - f(\omega_i, \omega_s) e^{-i(\omega_s - \omega_i)\tau}] \right|^2. \quad (9)$$

The second one is the HOM interference with two independent heralded single-photon sources, with a typical experimental setup shown in Refs. [67, 68]. In this interference, two signals s_1 and s_2 are sent to a beamsplitter for interference, and two idlers i_1 and i_2 are detected by single-photon detectors for heralding the signals. The four-fold coincidence counts P_4 as a function of τ can be described by [65, 66]

$$P_4(\tau) = \frac{1}{4} \int_0^\infty \int_0^\infty \int_0^\infty \int_0^\infty d\omega_{s_1} d\omega_{s_2} d\omega_{i_1} d\omega_{i_2} \left| f_1(\omega_{s_1}, \omega_{i_1}) f_2(\omega_{s_2}, \omega_{i_2}) - f_1(\omega_{s_2}, \omega_{i_1}) f_2(\omega_{s_1}, \omega_{i_2}) e^{-i(\omega_{s_2} - \omega_{s_1})\tau} \right|^2, \quad (10)$$

where f_1 and f_2 are the JSAs from the first and the second crystals.

We choose BiTaO₃, LGSe, and PMN-0.38PT as examples to test the HOM interference. Figure 3 (a) shows JSA figure is generated from BiTaO₃ crystal, which is under the GVM_1 condition. BiTaO₃ crystal is a uniaxial QPM crystal. The JSA is obtained by using a pump laser with a bandwidth of $\Delta\lambda = 4$ nm, and a crystal length L of 100 mm. The JSA has a long stripe shape along the horizontal axis. As for the spectral distributions of the signal and the idler photons, we can obtain them by projecting the joint spectral intensity onto the horizontal and vertical axes. The FWHM of the signal (idler) is 27.02 nm (0.92 nm). Figure 3 (c) shows the HOM pattern of two signals heralded by two idlers, the FWHM is 726.87 fs with visibility of 96.68%. Figure 3 (d) shows the HOM pattern of two heralded idlers with an FWHM of 8.74 ps and a visibility of 96.68%.

For the GVM_2 condition, the result is on the second row of Fig. 3. We investigate a biaxial BPM crystal LGSe. The JSA shape is also a long stripe, but it locates along the vertical axis. The pump bandwidth $\Delta\lambda$ and the crystal length L of Fig.3 (e) are 8 nm and 200 mm. The FWHM of the signal (idler) is 5.17 nm (75.40 nm) for Fig.3 (f). The FWHM of the HOM pattern by two heralded signals (idler) is 12.46 ps (1.17 ps), and the visibility is 97.05%, as shown in Fig.3 (g)(h).

For the GVM_3 condition, the result is on the third row of Fig. 3. We concentrate on PMN-0.38PT crystal.

This crystal has been studied before, however, it only focuses on the GVM₁ and GVM₂ conditions [22]. Here we make a thorough study of the GVM₃ condition. In this case, the JSA shape is near-round, and the spectra of the signal and idler are almost equal. Figure 3 (i) is obtained by using a pump bandwidth of $\Delta\lambda = 11$ nm, and a crystal length L of 100 mm. The spectra of the signal and idler have the same FWHM of 54.64 nm. The HOM interference from two independent signal or idler sources manifests the same performance with the FWHM of 12.24 ps and visibility of 82.33%, which is much lower than the GVM₁ and GVM₂ case. In the case of two-fold HOM interference, the visibility is 100% and the FWHM of the HOM pattern is 2.20 ps for Fig.3 (l).

IV. DISCUSSION

We summarize the result of all the BPM crystals in Fig. 4. The left vertical axis of the figure denotes the GVM condition and the corresponding PMF angle θ_{PMF} . The right vertical axis shows the maximal purity. The horizontal axis shows a wavelength range from 0 to 12 μm . Most of the crystals are located on the MIR band, from 2 μm to 12 μm . There are three cases on the NIR band. We also conclude the results of QPM crystals in Figure 5, which shows the down-converted wavelength, the poling period, and the maximal purity for all the results we calculated above.

It is important to discuss the detection of the single photons in the MIR region. Recent work shows that superconducting nanowire single-photon detectors (SNSPD) which have the best performance (98%) in the NIR band [69], while having a detection efficiency at MIR band of 70% at 2 μm [70], 40% at 2.5 μm and 10% at 3 μm [71], 1.64% for free-space communication [30]; upconversion detectors module combine with SAPD method demonstrates the efficiency of 6.5% in room temperature [14]; semiconductor photodiodes likes Cd admixture, graphene, black arsenic phosphorus, black phosphorus carbide, tellurene, PtSe₂ and PdSe₂ are good candidates for wide detection range [72]. See a recent review about MIR single-photon detection in [73]. In the future, developing new material for SNSPD and a more effective nonlinear process of upconversion for MIR detection will

be promising.

Expect from the 22 crystals we discussed above, we still find 6 kinds of new crystals in the MIR band: BGS, BGSe, BGGs, BGGSe, BGSS, and BGSSe [74–78]. They can be written as BaGa₄X₇ ($X=S, \text{Se}$) and BaGa₂MX₆ ($M = \text{Si, Ge}; X=S, \text{Se}$). Since the d_{eff} calculated and phase-matched method of these crystals is complex [79–83], we did not discuss them in this work. The d_{eff} for BGS and BGSe has been investigated in [84]. The d_{33} for BGGs, BGGSe, BGSS, and BGSSe is $-12.0, -23.0, 8.4, \text{ and } 12.3$ pm/V, respectively [85]. Moreover, the doping method can be utilized as a degree of freedom to manipulate the single-photon state at the MIR range [24].

For the GVM₃ condition, the purity can be further improved from 0.82 to near 1 using the custom poling crystal scheme, for example by machine learning method or metaheuristic algorithm [25, 86].

V. CONCLUSION

In conclusion, we have theoretically investigated 22 nonlinear optical crystals for MIR photon generation. The down-converted photons wavelength range is from 1298 nm (1224 nm) to 11650 nm (7944 nm) for the BPM (QPM) crystals. The corresponding purity for three kinds of GVM conditions are around 0.97, 0.97, and 0.82, respectively. The wavelength nondegenerated condition, the 4-fold HOM interference, and the 2-fold HOM interference are calculated in detail. This study may be helpful to the study of quantum communication, quantum imaging, and quantum metrology at MIR range.

ACKNOWLEDGMENTS

We thank Prof. Keiichi Edamatsu for the helpful discussions. This work is supported by the National Natural Science Foundations of China (Grant Nos.12074299, 91836102, 11704290), the Guangdong Provincial Key Laboratory (Grant No. GKLQSE202102), the Natural Science Foundation of Hubei Province (2022CFA039), and the JST SPRING (Grant Number JPM.JSP2114).

[1] M. Ebrahim-Zadeh and I. T. Sorokina, eds., *Mid-Infrared Coherent Sources and Applications* (Springer Science & Business Media, 2008).

[2] E. Tournie and L. Cerutti, eds., *Mid-infrared optoelectronics materials, devices, and applications* (Woodhead Publishing, 2019).

[3] I. A. Walmsley and M. G. Raymer, Toward quantum-information processing with photons, *Science* **307**, 1733 (2005).

[4] S. Slussarenko and G. J. Pryde, Photonic quantum information processing: A concise review, *Appl. Phys. Rev.* **6**, 041303 (2019).

[5] D. Caffey, M. B. Radunsky, V. Cook, M. Weida, P. R. Buerki, S. Crivello, and T. Day, Recent results from broadly tunable external cavity quantum cascade lasers, in *Novel In-Plane Semiconductor Lasers X*, Vol. 7953, edited by A. A. Belyanin and P. M. Smowton, International Society for Optics and Photonics (SPIE, 2011) pp. 336 – 346.

- [6] R. S. E. Shamy, D. Khalil, and M. A. Swillam, Mid-infrared optical gas sensor using plasmonic Mach-Zehnder interferometer, *Sci. Rep.* **10**, 1293 (2020).
- [7] K. Chen, S. Liu, B. Zhang, Z. Gong, Y. Chen, M. Zhang, H. Deng, M. Guo, F. Ma, F. Zhu, and Q. Yu, Highly sensitive photoacoustic multi-gas analyzer combined with mid-infrared broadband source and near-infrared laser, *Opt. Lasers Eng.* **124**, 105844 (2020).
- [8] L. Høgstedt, J. S. Dam, A.-L. Sahlberg, Z. Li, M. Aldén, C. Pedersen, and P. Tidemand-Lichtenberg, Low-noise mid-IR upconversion detector for improved R-degenerate four-wave mixing gas sensing, *Opt. Lett.* **39**, 5321 (2014).
- [9] G. J. Edelman, R. J. Hoveling, M. Roos, T. G. van Leeuwen, and M. C. Aalders, Infrared imaging of the crime scene: Possibilities and pitfalls, *Journal of Forensic Sciences* **58**, 1156 (2013).
- [10] J. Shi, T. T. W. Wong, Y. He, L. Li, R. Zhang, C. S. Yung, J. Hwang, K. Maslov, and L. V. Wang, High-resolution, high-contrast mid-infrared imaging of fresh biological samples with ultraviolet-localized photoacoustic microscopy, *Nat. Photonics* **13**, 609 (2019).
- [11] J. Yin, Y. Cao, Y.-H. Li, S.-K. Liao, L. Zhang, J.-G. Ren, W.-Q. Cai, W.-Y. Liu, B. Li, H. Dai, G.-B. Li, Q.-M. Lu, Y.-H. Gong, Y. Xu, S.-L. Li, F.-Z. Li, Y.-Y. Yin, Z.-Q. Jiang, M. Li, J.-J. Jia, G. Ren, D. He, Y.-L. Zhou, X.-X. Zhang, N. Wang, X. Chang, Z.-C. Zhu, N.-L. Liu, Y.-A. Chen, C.-Y. Lu, R. Shu, C.-Z. Peng, J.-Y. Wang, and J.-W. Pan, Satellite-based entanglement distribution over 1200 kilometers, *Science* **356**, 1140 (2017).
- [12] S. Wang, Z.-Q. Yin, D.-Y. He, W. Chen, R.-Q. Wang, P. Ye, Y. Zhou, G.-J. Fan-Yuan, F.-X. Wang, W. Chen, Y.-G. Zhu, P. V. Morozov, A. V. Divochiy, Z. Zhou, G.-C. Guo, and Z.-F. Han, Twin-field quantum key distribution over 830-km fibre, *Nat. Photonics* **16**, 154 (2022).
- [13] L. Zhou, Y.-B. Sheng, and G.-L. Long, Device-independent quantum secure direct communication against collective attacks, *Sci. Bull.* **65**, 12 (2020).
- [14] M. Mancinelli, A. Trenti, S. Piccione, G. Fontana, J. S. Dam, P. Tidemand-Lichtenberg, C. Pedersen, and L. Pavesi, Mid-infrared coincidence measurements on twin photons at room temperature, *Nat. Commun.* **8**, 15184 (2017).
- [15] Y. M. Sua, H. Fan, A. Shahverdi, J.-Y. Chen, and Y.-P. Huang, Direct generation and detection of quantum correlated photons with 3.2 μm wavelength spacing, *Sci. Rep.* **7**, 17494 (2017).
- [16] M. Arahata, Y. Mukai, B. Cao, T. Tashima, R. Okamoto, and S. Takeuchi, Wavelength variable generation and detection of photon pairs in visible and mid-infrared regions via spontaneous parametric downconversion, *J. Opt. Soc. Am. B* **38**, 1934 (2021).
- [17] P. S. Kuo, P. G. Schunemann, M. V. Camp, V. B. Verma, T. Gerrits, S. W. Nam, and R. P. Mirin, Towards a source of entangled photon pairs in gallium phosphide, in *Conference on Lasers and Electro-Optics* (Optical Society of America, 2019) p. FTh1D.5.
- [18] L. M. Rosenfeld, D. A. Sulway, G. F. Sinclair, V. Anant, M. G. Thompson, J. G. Rarity, and J. W. Silverstone, Mid-infrared quantum optics in silicon, *Opt. Express* **28**, 37092 (2020).
- [19] S. Prabhakar, T. Shields, A. C. Dada, M. Ebrahim, G. G. Taylor, D. Morozov, K. Erotokritou, S. Miki, M. Yabuno, H. Terai, C. Gawith, M. Kues, L. Caspani, R. H. Hadfield, and M. Clerici, Two-photon quantum interference and entanglement at 2.1 μm , *Sci. Adv.* **6**, eaay5195 (2020).
- [20] M. Hojo and K. Tanaka, Broadband infrared light source by simultaneous parametric down-conversion, *Sci. Rep.* **11**, 10.1038/s41598-021-97531-w (2021).
- [21] K. J. Lee, S. Lee, and H. Shin, Extended phase-matching properties of periodically poled potassium niobate crystals for mid-infrared polarization-entangled photon-pair generation, *Appl. Opt.* **55**, 9791 (2016).
- [22] D. Kundys, F. Graffitti, R. A. McCracken, A. Fedrizzi, and B. Kundys, Numerical study of reconfigurable mid-ir single photon sources based on functional ferroelectrics, *Adv. Quant. Technol.* **3**, 1900092 (2020).
- [23] R. A. McCracken, F. Graffitti, and A. Fedrizzi, Numerical investigation of mid-infrared single-photon generation, *J. Opt. Soc. Am. B* **35**, C38 (2018).
- [24] B. Wei, W.-H. Cai, C. Ding, G.-W. Deng, R. Shimizu, Q. Zhou, and R.-B. Jin, Mid-infrared spectrally-uncorrelated biphotons generation from doped PPLN: a theoretical investigation, *Opt. Express* **29**, 256 (2021).
- [25] W.-H. Cai, Y. Tian, S. Wang, C. You, Q. Zhou, and R.-B. Jin, Optimized design of the lithium niobate for spectrally-pure-state generation at mid wavelengths using metaheuristic algorithm, *Adv. Quant. Technol.* **5**, 2200028 (2022).
- [26] J.-L. Zhu, W.-X. Zhu, X.-T. Shi, C.-T. Zhang, X. Hao, Z.-X. Yang, and R.-B. Jin, Design of mid-infrared entangled photon sources using lithium niobate, *J. Opt. Soc. Am. B* **40**, A9 (2023).
- [27] C.-T. Zhang, X.-T. Shi, W.-X. Zhu, J.-L. Zhu, X.-Y. Hao, and R.-B. J. and, Preparation of spectrally pure single-photon source at 3 μm mid-infrared band from lithium niobate crystal with domain sequence algorithm, *Acta Phys. Sin.* **71**, 204201 (2022).
- [28] R. Razali, Z. Ikonić, D. Indjin, and P. Harrison, Polarization-entangled mid-infrared photon generation in p-doped semiconductor quantum wells, *Semicond. Sci. Technol.* **31**, 115011 (2016).
- [29] F. Marsili, F. Bellei, F. Najafi, A. E. Dane, E. A. Dauler, R. J. Molnar, and K. K. Berggren, Efficient single photon detection from 500 nm to 5- μm wavelength, *Nano Letters* **12**, 4799 (2012).
- [30] F. Bellei, A. P. Cartwright, A. N. McCaughan, A. E. Dane, F. Najafi, Q. Zhao, and K. K. Berggren, Free-space-coupled superconducting nanowire single-photon detectors for infrared optical communications, *Opt. Express* **24**, 3248 (2016).
- [31] P. S. Kuo, Using silica fiber coupling to extend superconducting nanowire single-photon detectors into the infrared, *OSA Continuum* **1**, 1260 (2018).
- [32] S. Piccione, M. Mancinelli, A. Trenti, G. Fontana, J. Dam, P. Tidemand-Lichtenberg, C. Pedersen, and L. Pavesi, Mid-infrared coincidence measurements based on intracavity frequency conversion, in *Nonlinear Frequency Generation and Conversion: Materials and Devices XVII*, Vol. 10516, edited by K. L. Vodopyanov and K. L. Schepler, International Society for Optics and Photonics (SPIE, 2018) pp. 251 – 258.
- [33] W. P. Grice, A. B. U'Ren, and I. A. Walmsley, Eliminating frequency and space-time correlations in multiphoton states, *Phys. Rev. A* **64**, 063815 (2001).
- [34] K. Kato, High-power difference-frequency generation at 4.4-5.7 μm in LiIO_3 , *IEEE J. Quant. Elec.* **21**, 119 (1985).

- [35] K. Kato, V. Petrov, and N. Umemura, Phase-matching properties of yellow color HgGa_2S_4 for SHG and SFG in the 0.944–10.5910 μm range, *Appl. Opt.* **55**, 3145 (2016).
- [36] G. C. Bhar, Refractive index interpolation in phase-matching, *Applied Optics* **15**, 305.1 (1976).
- [37] K. Kato, F. Tanno, and N. Umemura, Sellmeier and thermo-optic dispersion formulas for GaSe (revisited), *Appl. Opt.* **52**, 2325 (2013).
- [38] S. Fossier, S. Salaün, J. Mangin, O. Bidault, I. Thénot, J.-J. Zondy, W. Chen, F. Rotermund, V. Petrov, P. Petrov, J. Henningsen, A. Yelisseyev, L. Isaenko, S. Lobanov, O. Balachninaite, G. Sleky, and V. Sirutkaitis, Optical, vibrational, thermal, electrical, damage, and phase-matching properties of lithium thioindate, *J. Opt. Soc. Am. B* **21**, 1981 (2004).
- [39] K. Kato, V. Petrov, and N. Umemura, Sellmeier and thermo-optic dispersion formulas for LiInSe_2 , *Appl. Opt.* **53**, 1063 (2014).
- [40] V. Petrov, J.-J. Zondy, O. Bidault, L. Isaenko, V. Vedenyapin, A. Yelisseyev, W. Chen, A. Tyazhev, S. Lobanov, G. Marchev, and D. Kolker, Optical, thermal, electrical, damage, and phase-matching properties of lithium selenoindate, *J. Opt. Soc. Am. B* **27**, 1902 (2010).
- [41] K. Kato, K. Miyata, L. Isaenko, S. Lobanov, V. Vedenyapin, and V. Petrov, Phase-matching properties of LiGaS_2 in the 1.025–10.5910 μm spectral range, *Opt. Lett.* **42**, 4363 (2017).
- [42] V. Petrov, A. Yelisseyev, L. Isaenko, S. Lobanov, A. Titov, and J.-J. Zondy, Second harmonic generation and optical parametric amplification in the mid-IR with orthorhombic biaxial crystals LiGaS_2 and LiGaSe_2 , *Appl. Phys. B* **78**, 543 (2004).
- [43] K. Miyata, V. Petrov, and K. Kato, Phase-matching properties of LiGaSe_2 for SHG and SFG in the 1.026–10.5910 μm range, *Appl. Opt.* **56**, 6126 (2017).
- [44] I. Dolev, A. Ganany-Padowicz, O. Gayer, A. Arie, J. Mangin, and G. Gadret, Linear and nonlinear optical properties of $\text{MgO}:\text{LiTaO}_3$, *Appl. Phys. B* **96**, 423 (2009).
- [45] M. V. Pack, D. J. Armstrong, and A. V. Smith, Measurement of the $\chi(2)$ tensor of the potassium niobate crystal, *J. Opt. Soc. Am. B* **20**, 2109 (2003).
- [46] C. He, W. Ge, X. Zhao, H. Xu, H. Luo, and Z. Zhou, Wavelength dependence of electro-optic effect in tetragonal lead magnesium niobate lead titanate single crystals, *J. Appl. Phys.* **100**, 113119 (2006).
- [47] W. J. Tropf, Temperature-dependent refractive index models for BaF_2 , CaF_2 , MgF_2 , SrF_2 , LiF , NaF , KCl , ZnS , and ZnSe , *Opt. Eng.* **34**, 1369 (1995).
- [48] V. G. Dmitriev, G. G. Gurzadyan, and D. N. Nikogosyan, *Handbook of Nonlinear Optical Crystals*, 3rd ed. (Springer-Verlag Berlin Heidelberg, 1999).
- [49] D. N. Nikogosyan, *Nonlinear Optical Crystals: A Complete Survey* (Springer-Verlag, 2005).
- [50] F. Wang, Calculation of the electro-optical and nonlinear optical coefficients of ferroelectric materials from their linear properties, *Phys. Rev. B* **59**, 9733 (1999).
- [51] P. J. Mosley, J. S. Lundeen, B. J. Smith, and I. A. Walmsley, Conditional preparation of single photons using parametric downconversion: a recipe for purity, *New J. of Phys.* **10**, 093011 (2008).
- [52] R.-B. Jin, W.-H. Cai, C. Ding, F. Mei, G.-W. Deng, R. Shimizu, and Q. Zhou, Spectrally uncorrelated biphotons generated from "the family of BBO crystal", *Quantum Eng.* **2**, e38 (2020).
- [53] R.-B. Jin, R. Shimizu, K. Wakui, H. Benichi, and M. Sasaki, Widely tunable single photon source with high purity at telecom wavelength, *Opt. Express* **21**, 10659 (2013).
- [54] R.-B. Jin, N. Cai, Y. Huang, X.-Y. Hao, S. Wang, F. Li, H.-Z. Song, Q. Zhou, and R. Shimizu, Theoretical investigation of a spectrally pure-state generation from isomorphs of KDP crystal at near-infrared and telecom wavelengths, *Phys. Rev. Appl.* **11**, 034067 (2019).
- [55] F. Graffitti, J. Kelly-Massicotte, A. Fedrizzi, and A. M. Branczyk, Design considerations for high-purity heralded single-photon sources, *Phys. Rev. A* **98**, 053811 (2018).
- [56] N. Quesada and A. M. Branczyk, Gaussian functions are optimal for waveguided nonlinear-quantum-optical processes, *Phys. Rev. A* **98**, 043813 (2018).
- [57] A. Smith, SNLO, <http://www.as-photonics.com/snlo>.
- [58] A. V. Smith, *Crystal nonlinear optics: with SNLO examples* (AS-Photonics Albuquerque, NM, USA, 2018).
- [59] D. S. Hum and M. M. Fejer, Quasi-phase-matching, *Comptes Rendus Physique* **8**, 180 (2007).
- [60] R. Shimizu and K. Edamatsu, High-flux and broadband biphoton sources with controlled frequency entanglement, *Opt. Express* **17**, 16385 (2009).
- [61] T. Wang, P. Chen, C. Xu, Y. Zhang, D. Wei, X. Hu, G. Zhao, M. Xiao, and S. Zhu, Periodically poled LiNbO_3 crystals from 1D and 2D to 3D, *Sci. China Technol. Sci.*, s11431 (2020).
- [62] R.-B. Jin, P. Zhao, P. Deng, and Q.-L. Wu, Spectrally pure states at telecommunications wavelengths from periodically poled MTiOXO_4 ($M = \text{K, Rb, Cs}$; $X = \text{P, As}$) crystals, *Phys. Rev. Appl.* **6**, 064017 (2016).
- [63] C. K. Hong, Z. Y. Ou, and L. Mandel, Measurement of subpicosecond time intervals between two photons by interference, *Phys. Rev. Lett.* **59**, 2044 (1987).
- [64] W. P. Grice and I. A. Walmsley, Spectral information and distinguishability in type-II down-conversion with a broadband pump, *Phys. Rev. A* **56**, 1627 (1997).
- [65] Z.-Y. J. Ou, *Multi-Photon Quantum Interference* (Springer, 2007).
- [66] R.-B. Jin, T. Gerrits, M. Fujiwara, R. Wakabayashi, T. Yamashita, S. Miki, H. Terai, R. Shimizu, M. Takeoka, and M. Sasaki, Spectrally resolved Hong-Ou-Mandel interference between independent photon sources, *Opt. Express* **23**, 28836 (2015).
- [67] P. J. Mosley, J. S. Lundeen, B. J. Smith, P. Wasylczyk, A. B. U'Ren, C. Silberhorn, and I. A. Walmsley, Heralded generation of ultrafast single photons in pure quantum states, *Phys. Rev. Lett.* **100**, 133601 (2008).
- [68] R.-B. Jin, K. Wakui, R. Shimizu, H. Benichi, S. Miki, T. Yamashita, H. Terai, Z. Wang, M. Fujiwara, and M. Sasaki, Nonclassical interference between independent intrinsically pure single photons at telecommunication wavelength, *Phys. Rev. A* **87**, 063801 (2013).
- [69] D. V. Reddy, R. R. Nerem, S. W. Nam, R. P. Mirin, and V. B. Verma, Superconducting nanowire single-photon detectors with 98% system detection efficiency at 1550 nm, *Optica* **7**, 1649 (2020).
- [70] J. Chang, J. W. N. Los, R. Gourgues, S. Steinhauer, S. N. Dorenbos, S. F. Pereira, H. P. Urbach, V. Zwiller, and I. E. Zadeh, Efficient mid-infrared single-photon detection using superconducting nbtin nanowires with high time resolution in a gifford-mcmahon cryocooler, *Photon.*

- Res.* **10**, 1063 (2022).
- [71] P. I. Zolotov, A. V. Divochiy, Y. B. Vakhtomin, P. V. Morozov, V. A. Seleznev, and K. V. Smirnov, Development of high-effective superconducting single-photon detectors aimed for mid-IR spectrum range, *Journal of Physics: Conference Series* **917**, 062037 (2017).
- [72] M. Long, P. Wang, H. Fang, and W. Hu, Progress, challenges, and opportunities for 2D material based photodetectors, *Adv. Funct. Mat.* **29**, 1803807 (2018).
- [73] S. Dello Russo, A. Elefante, D. Dequal, D. K. Pallotti, L. Santamaria Amato, F. Sgobba, and M. Siciliani de Cumis, Advances in mid-infrared single-photon detection, *Photonics* **9**, 10.3390/photonics9070470 (2022).
- [74] X. Li, C. Li, P. Gong, Z. Lin, J. Yao, and Y. Wu, BaGa₂SnSe₆: a new phase-matchable IR nonlinear optical material with strong second harmonic generation response, *J. Mater. Chem. C* **3**, 10998 (2015).
- [75] N. Zhai, C. Li, B. Xu, L. Bai, J. Yao, G. Zhang, Z. Hu, and Y. Wu, Temperature-dependent sellmeier equations of IR nonlinear optical crystal BaGa₄Se₇, *Crystals* **7**, 62 (2017).
- [76] Y. He, Y. Guo, D. Xu, Y. Wang, X. Zhu, J. Yao, C. Yan, L. Tang, J. Li, K. Zhong, C. Liu, X. Fan, Y. Wu, and J. Yao, High energy and tunable mid-infrared source based on BaGa₄Se₇ crystal by single-pass difference-frequency generation, *Opt. Express* **27**, 9241 (2019).
- [77] K. Kato, V. V. Badikov, L. Wang, V. L. Panyutin, K. V. Mitin, K. Miyata, and V. Petrov, Effective nonlinearity of the new quaternary chalcogenide crystal BaGa₂GeSe₆, *Opt. Lett.* **45**, 2136 (2020).
- [78] U. Elu, L. Maidment, L. Vamos, T. Steinle, F. Haberstroh, V. Petrov, V. Badikov, D. Badikov, and J. Biegert, Few-cycle mid-infrared pulses from BaGa₂GeSe₆, *Opt. Lett.* **45**, 3813 (2020).
- [79] E. Boursier, P. Segonds, J. Debray, P. L. Inácio, V. Panyutin, V. Badikov, D. Badikov, V. Petrov, and B. Boulanger, Angle noncritical phase-matched second-harmonic generation in the monoclinic crystal BaGa₄Se₇, *Opt. Lett.* **40**, 4591 (2015).
- [80] E. Boursier, P. Segonds, B. Ménaert, V. Badikov, V. Panyutin, D. Badikov, V. Petrov, and B. Boulanger, Phase-matching directions and refined sellmeier equations of the monoclinic acentric crystal BaGa₄Se₇, *Opt. Lett.* **41**, 2731 (2016).
- [81] K. Kato, K. Miyata, and V. Petrov, Phase-matching properties of BaGa₄Se₇ for SHG and SFG in the 0.901–10.5910μm range, *Appl. Opt.* **56**, 2978 (2017).
- [82] K. Kato, K. Miyata, V. V. Badikov, and V. Petrov, Phase-matching properties of BaGa₂GeSe₆ for three-wave interactions in the 0.778–10.5910μm spectral range, *Appl. Opt.* **57**, 7440 (2018).
- [83] P. Liu, L. Guo, F. Qi, W. Li, W. Li, Q. Fu, J. Yao, M. Xia, Z. Liu, and Y. Wang, Large dynamic range and wideband mid-infrared upconversion detection with BaGa₄Se₇ crystal, *Optica* **9**, 50 (2022).
- [84] V. Badikov, D. Badikov, G. Shevyrdayeva, A. Tyazhev, G. Marchev, V. Panyutin, V. Petrov, and A. Kwasniewski, Phase-matching properties of BaGa₄S₇ and BaGa₄Se₇: Wide-bandgap nonlinear crystals for the Mid-Infrared, in *Advances in Optical Materials* (Optical Society of America, 2011) p. JWB4.
- [85] W. Yin, K. Feng, R. He, D. Mei, Z. Lin, J. Yao, and Y. Wu, BaGa₂MQ₆ (M = Si, Ge; Q = S, Se): a new series of promising IR nonlinear optical materials, *Dalton Transactions* **41**, 5653 (2012).
- [86] C. Cui, R. Arian, S. Guha, N. Peyghambarian, Q. Zhuang, and Z. Zhang, Wave-function engineering for spectrally uncorrelated biphotons in the telecommunication band based on a machine-learning framework, *Phys. Rev. Appl.* **12**, 034059 (2019).